



# X-ray mirror figure correction by differential deposition and off-line metrology

Christian Morawe,\* Sylvain Labouré, Jean-Christophe Peffen, François Perrin, Amparo Vivo and Raymond Barrett

X-ray Optics Group, ESRF – The European Synchrotron, 71 Avenue des Martyrs, 38043 Grenoble, France.

\*Correspondence e-mail: morawe@esrf.fr

Received 4 July 2019

Accepted 3 September 2019

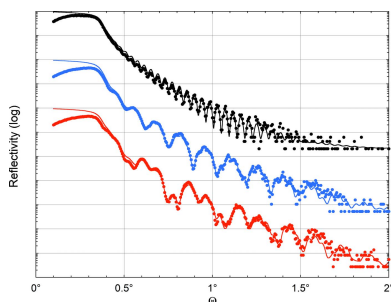
Edited by S. M. Heald, Argonne National Laboratory, USA

**Keywords:** X-ray optics; figure corrections; differential depositions; off-line metrology; magnetron sputtering.

The surface figure error of a hard X-ray mirror was improved by combining differential deposition and off-line metrology tools. Thin Cr layers were deposited on flat substrates by DC magnetron sputtering. The substrates were moved in front of a beam-defining aperture. The required velocity profile was calculated using a deconvolution algorithm. The Cr thickness profiles were measured directly using hard X-ray reflectivity data. The surface figure was characterized using conventional visible-light metrology instrumentation (long trace profiler) before and after the deposition. The method converges quickly, and after two iterations the mirror surface figure had improved by a factor of 7. The surface roughness evolves with increasing Cr thickness and deteriorates the quality of subsequent multilayer coatings. The mirror curvature can change upon coating, which complicates the interpretation of the surface metrology data. In this context, the role of layer stress is discussed. Potential improvements of the process are also proposed.

## 1. Introduction

The performance of reflective X-ray optics, in particular multilayer (ML) coated mirrors, strongly depends on the quality of the underlying substrates (Morawe *et al.*, 2011). Surface micro-roughness causes diffuse scattering and reduces the ML reflectance while figure errors alter the uniformity of the reflected beam or blur the spot of focusing devices. In modern synchrotron or free-electron laser light sources, figure accuracy requirements have evolved down to tolerances of 1 nm over mirror lengths of tens of centimetres (Yamauchi *et al.*, 2011). To correct for figure errors at these length scales, precise metrology and deterministic polishing techniques have been developed. The most prominent methods used for X-ray optics are elastic emission machining (EEM) (Yamauchi *et al.*, 2002), ion beam figuring (IBF) (Arnold *et al.*, 2010; Wang *et al.*, 2019) and differential deposition (DD). While EEM and IBF rely on material removal, DD adds material via thin-film coating. DD has been developed by the astronomy community to improve thin-shell payload mirrors (Kilaru *et al.*, 2011) but has also been applied to synchrotron optics (Handa *et al.*, 2008; Alcock & Cockerton, 2010; Matsuyama *et al.*, 2018). This work will focus on the correction of medium to long spatial-period height errors of X-ray mirror substrates with a potential length of up to 1 m. After the presentation of the method and the experimental techniques, results of a differentially coated mirror will be shown. The potential impact of film stress and roughness on the corrected substrates will be discussed and directions for further development will be indicated.



## 2. Methods and experimental techniques

### 2.1. Theoretical approach

In contrast to the very common dwell time approach (Atkins *et al.*, 2015), where the substrate is moved in small steps and remains stationary during a given amount of time, the method applied here is based on continuous substrate motion. The one-dimensional thickness distribution  $t(x_s)$  of a film deposited on a substrate moving in front of a particle source can be written in the following way (Morawe & Peffen, 2009),

$$t(x_s) = \int_{-S}^{+S} R f(x_m - x_s) \frac{dx_m}{v(x_m)}. \quad (1)$$

Here,  $f(x_m - x_s)$  is the normalized steady-state flux profile of the source at the substrate surface,  $R$  the deposition rate at its centre and  $v(x_m)$  the local speed. The variable  $x_s$  refers to substrate coordinates,  $x_m$  is the motor driver position. The integration is carried out over the full stroke  $2S$  of the substrate motion. The convolution operation of equation (1) can be solved easily when the experimental parameters  $R$  and  $f$  are known and when the speed profile  $v$  can be chosen to obtain  $t$ . However, in the present case the thickness distribution  $t$  is given and the speed profile  $v$  needs to be calculated, which corresponds to a deconvolution process. Using discrete steps, equation (1) can be written in the form of a matrix multiplication as a system of linear equations. An algorithm based on matrix inversion was developed to solve the problem. It includes sub-routines that were originally developed for astronomical image deconvolution by NASA (Varosi, 1992). The deposition rate  $R$  and the flux profile  $f$  can be measured experimentally and used as input parameters for the optimization programme.

### 2.2. Thin-film deposition

All coatings were made at the ESRF ML deposition facility (Morawe *et al.*, 2007) using DC magnetron sputtering. The deposition process took place in an Ar atmosphere at a working pressure of 0.1 Pa. Cr was deposited with a power of 100 W and a deposition rate of about  $0.3 \text{ nm s}^{-1}$ . A beam-defining aperture with an opening of 24 mm was placed 7.5 mm in front of the substrate surface and about 60 mm away from the rectangular sputter target. The sample can be mounted with an accuracy of 0.1–0.2 mm with respect to the cathode position. Static Cr coatings, where the thickness is controlled by opening and closing a fast shutter, were carried out to measure the particle flux distribution in the substrate plane. The corrective coatings were made in dynamic mode where the substrate moves in front of the aperture following a pre-programmed velocity profile. Repeated duty cycles (back and forth motions) can be applied to obtain the required thickness profile, which better distributes the thermal load on the substrate and allows for mechanically convenient velocity values. Under the given conditions, the substrate temperature does not exceed  $100^\circ\text{C}$ .

### 2.3. X-ray reflectivity (XRR)

All coatings were characterized on a laboratory X-ray reflectometer with a microfocus Cu tube at 8048 eV (Morawe *et al.*, 2018). The instrument can be operated at medium resolution with a Montel-type ML collimator, or in high-resolution mode by inserting a Si(111) double-crystal monochromator further downstream. Specular reflectivity data can be taken with a dynamical range of up to  $10^7$ . To measure thin films with strongly varying thickness the X-ray beam can be oriented perpendicular to the thickness gradient and slit down to minimize its impact on the reflectivity data. The positioning accuracy of the sample on the instrument is of the order of 0.1 mm. Simulation software based on the Parratt formalism (Parratt, 1954) allows for the precise determination of thicknesses, mass densities and interface widths.

### 2.4. Long trace profiler (LTP)

The ESRF LTP (Rommeveaux *et al.*, 2008) is an in-house deflectometer used to perform meridional measurements on planar or non-planar surfaces, up to 1.4 m long, with an accuracy of  $0.1 \mu\text{rad}$  and a lateral resolution of 2 mm. Based on the pencil-beam deflectometry technique, an elementary scan yields the slope variation along a single line. The mirror coordinate system reference with respect to the mirror edges is obtained with a precision better than  $50 \mu\text{m}$  using the LTP signal detection. The mirror is supported by two rods spaced by half of its length in order to analytically subtract gravity effects. The integration of the slope profile allows retrieval of the height profile of the mirror. In the case of a flat, a sphere or a tangential cylinder, the residual shape error profile is then obtained by subtracting a second-order polynomial from the measured height profile.

### 2.5. Micro interferometer

The surface roughness was investigated using a Wyko NT9300 white-light interferometer. Three parfocal objectives ( $50\times$ ,  $5\times$  and  $2.5\times$ ) are available on the automated turret offering respective optical resolutions of  $0.5 \mu\text{m}$ ,  $2.2 \mu\text{m}$  and  $3.8 \mu\text{m}$ . The instrument is also equipped with encoded and motorized  $X$  and  $Y$  translation stages. The accuracy of the translation allows tracking of the same measurement point after repositioning the mirror provided two fiducial markers can be identified, thus allowing rigorous follow up of the evolution of the micro-roughness in a spatial frequency domain from about  $0.4 \text{ mm}^{-1}$  to  $2 \mu\text{m}^{-1}$  at different stages of the DD process.

### 2.6. Scanning electron microscopy (SEM)

Surface imaging was performed at the ESRF Microimaging Laboratory using a LEO 1530 scanning electron microscope in secondary electron contrast mode.

### 2.7. Stress measurements

The residual stress of the thin films was studied by recording the change of the macroscopic sample curvature and by

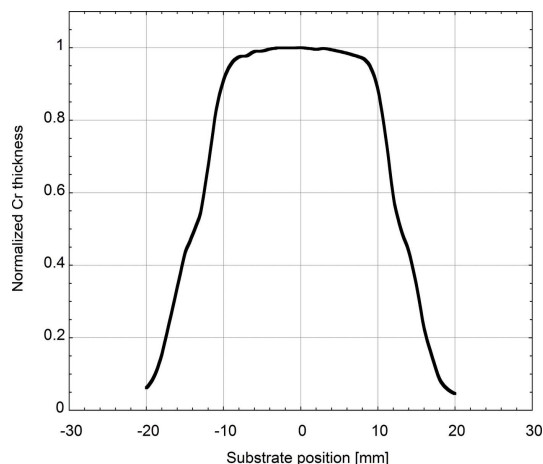


**Figure 1**  
Normalized thickness profile of a Cr film coated on a stationary substrate.

applying the Stoney equation (Stoney, 1909). The curvature evolution was measured quasi *in situ* using a specific monitor (Morawe *et al.*, 2010).

### 3. Experimental results

#### 3.1. Static flux distribution (SFD)

The first important step towards successful DD is to characterize the particle flux distribution  $f$  when the substrate rests stationary in front of the beam aperture. A 20 nm-thick Cr film was deposited on a Si wafer and its local thickness was measured with XRR in 1 mm steps across a total width of 40 mm. The normalized SFD is shown in Fig. 1. Its shape is nearly rectangular with a width of about 28 mm (full width at half-maximum) and two pronounced shoulders, which are images of the two straight erosion lines on the rectangular sputter target that are projected on the substrate right behind the edges of the beam-defining aperture.

#### 3.2. Differential test coating

To investigate the accuracy of the DD method, a specific thickness profile was chosen and used as a test target for the deconvolution algorithm. An oscillating function was generated along the total length of a 280 mm-long Si substrate [blue line in Fig. 2(a)]. The function contains seven nodes and a local periodicity decreasing from 160 mm at the left side to 60 mm at the right side of the mirror. Based on the measured SFD width of 28 mm, features smaller than 30 mm are not expected to be corrected. The profile thickness varies between 10 nm and 30 nm, which is a compromise between efficient figure correction with minimum thickness accumulation and the acceleration limits of the motion system.

The blue line in Fig. 2(b) indicates the speed profile returned by the deconvolution algorithm. The speed was forced to constant values near the points of reversal to provide convenient boundary conditions for the motion system. Speed variations between 3 and 20 mm s<sup>-1</sup> are required and seven full duty cycles were executed by the carrier. The expected

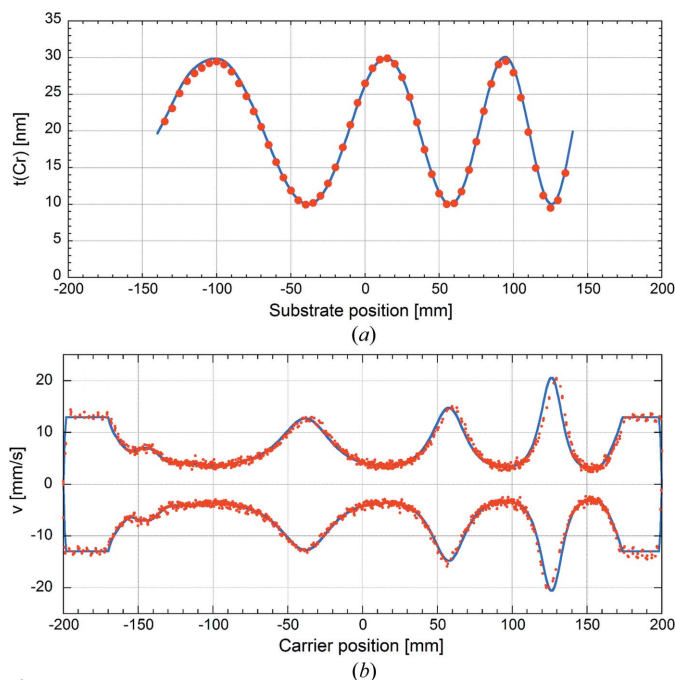


**Figure 2**  
(a) Target thickness profile (blue line) and XRR experimental result (red dots) versus position of a Cr test coating on a 280 mm-long Si substrate. (b) Corresponding calculated (blue line) and measured (red dots) speed profiles along the stroke of the substrate carrier. Full duty cycles (back and forth) were applied.

thickness profile after optimization (not shown here) agrees within less than 0.5 nm peak-to-valley (PV) or 0.075 nm root-mean-square (RMS) with the target profile. The red dots in Fig. 2(b) show the experimental speed data obtained from the encoder signal during the deposition process. The motion system follows the theoretical curve, except for regions of strong acceleration or deceleration. At low speed, considerable noise can be observed, which is caused by intrinsic motion errors of the carrier system. After the process, the Cr layer thickness was measured with XRR every 5 mm along a length of 270 mm. The red dots in Fig. 2(a) indicate the experimental outcome that agrees very well with the expected curve (blue line), both in thickness and position, within the estimated accuracy. The residual errors are below 1 nm (PV) and within  $\pm 2.5\%$  of the target values. This is an excellent result for an iterative correction process and corresponds to potential convergence rates of more than 95% per iteration.

#### 3.3. Figure correction of a mirror

As a first application, a 300 mm-long, 50 mm-wide and 20 mm-thick Pyrex glass mirror was selected. Its initial surface figure was characterized using the LTP. The measured height-error profile is displayed in Fig. 3 (black line).

The required corrective Cr thickness profile is shown in Fig. 4 (blue line). It was inserted as input data into the deconvolution algorithm to obtain the speed profile for the first iteration. As described in Section 3.2, the Cr layer thickness was measured with XRR in 5 mm steps along a length of 275 mm. The experimental data are shown as red

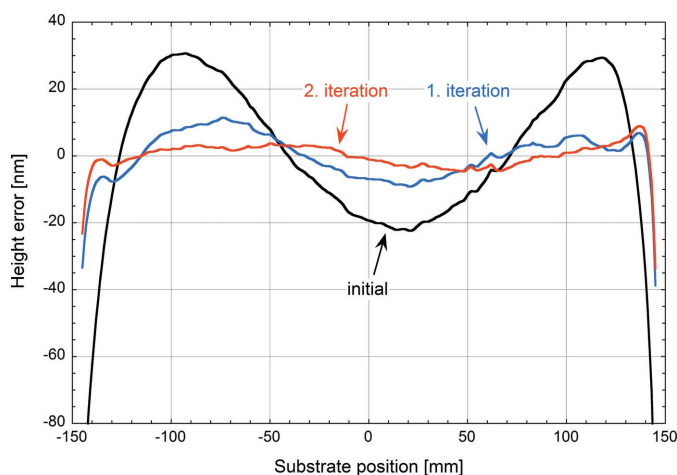


**Figure 3**  
LTP measured surface-height errors of the initial glass mirror (black line) and after the first (blue line) and second corrective Cr coating (red line).

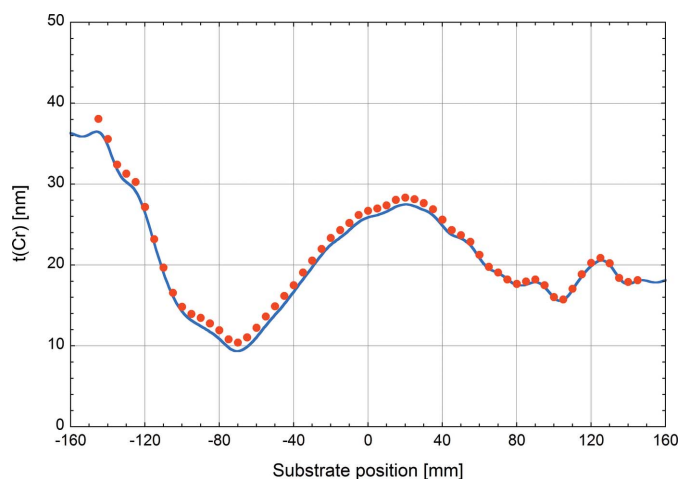


**Figure 5**  
Required Cr thickness profile (blue line) and XRR experimental data after the deposition (red dots) of the second corrective layer.

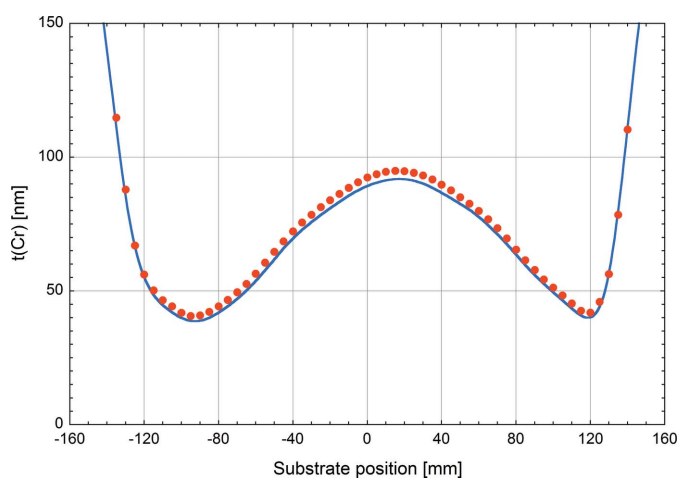


**Figure 4**  
Required Cr thickness profile (blue line) and XRR experimental data after the deposition (red dots) of the first corrective layer.

dots in Fig. 4. The residual thickness error is below 2.5 nm (PV), similar to what was achieved during the test in Section 3.2. After this first iteration the height-error profile was measured again. The corresponding LTP data are shown in Fig. 3 (blue line). Although the overall surface figure was improved by more than a factor of two, the residual height error clearly exceeds the level of 2.5 nm expected from the XRR data. The correction process was repeated following the same protocol and both the target Cr thickness profile and the XRR results are shown in Fig. 5. The residual thickness error drops below 1 nm (PV) in absolute numbers but remains near 2% of the target thickness as for the first iteration. Again, the surface figure was measured with the LTP, shown as the red line in Fig. 3. Despite another improvement by a factor of two, the observed residual height error remains significantly greater than the 1 nm accuracy expected from the XRR data.

To understand the observed discrepancy between XRR thickness and LTP height-error data the overall mirror figure was investigated. The profiles before (black solid line) and

after the two iterations (blue and red solid lines) are summarized in Fig. 6. One observes a considerable reduction in the overall mirror curvature after each iteration. Since the height-error profiles shown in Fig. 3 are obtained by removing the best-fit second-order function from the raw figure data, any change in the curvature can have a dramatic impact on the residual height error and therefore modify the metrology reference after each iteration. The dashed blue line indicates the expected figure after the first iteration (except for an arbitrary thickness offset). It corresponds to the initial height profile (black solid line in Fig. 6) minus the initial figure error (black solid line in Fig. 3). The solid blue line shows the experimental result after the first iteration that is clearly off the dashed blue curve. The difference is smaller after the second iteration, probably because the average Cr thickness has dropped compared with the first correction. Despite the observed curvature change the DD technique allowed, with only two iterations, a reduction in the figure error of the glass

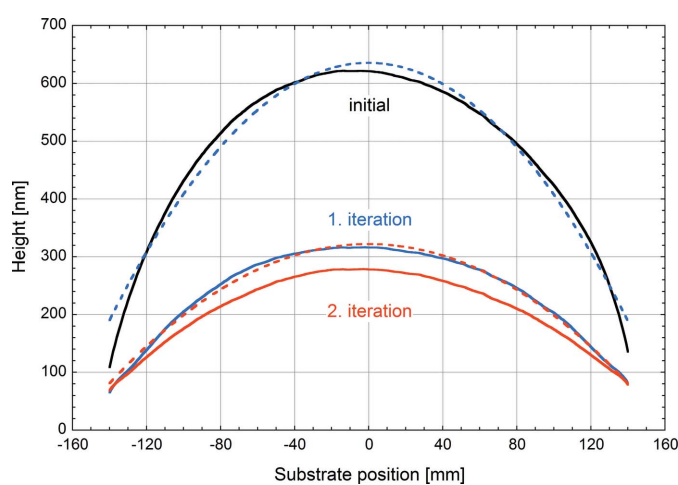


**Figure 6**  
LTP height profiles of the initial glass mirror (black solid line) and after the first (blue solid line) and second corrective Cr coating (red solid line). The blue dashed line indicates the expected figure after the first iteration, the red dashed line indicates the equivalent after the second iteration.

mirror along 280 mm from 93.1 nm (PV) or 19.9 nm (RMS) to 12.7 nm (PV) or 2.7 nm (RMS).

#### 4. Discussion

##### 4.1. XRR analysis

The use of XRR to measure the thickness profile of each corrective Cr coating is novel for such applications. The potential accuracy of this technique is very high, provided that the spectra can be resolved and interpreted correctly. With the present instrumentation, a Cr thickness of up to 100 nm can be resolved and measured with an accuracy of better than 1%, a situation that could be improved by better beam collimation and higher photon energies. When the total film thickness exceeds this limit, XRR is no longer capable of following the DD iterations. However, Cr coatings that are exposed to air for *ex situ* metrology form a thin oxide layer that produces X-ray optical contrast when overcoated with an additional Cr film. This effect allows XRR to be used for thickness measurements of the upper layer(s) even if the total accumulated Cr can no longer be resolved. Fig. 7 shows an example where three Cr layers were deposited on top of each other and exposed to air after each process. The initial layer (black data points) is with a 94 nm thickness close to the resolution limit of the reflectometer as can be seen from the narrow Kiessig fringes. After adding a 28 nm-thick layer (blue data points) the initial oscillations are damped and new broader fringes dominate the spectrum. The deposition of a third 14 nm-thick Cr layer (red data points) modifies the fringe pattern while maintaining their visibility. The respective simulated spectra are overlaid as solid lines in the corresponding colours. They confirm that even after three successive Cr coatings the XRR spectra can be analyzed with sufficient accuracy to extract the upper layer thickness. Instead of using the natural Cr surface

oxide as contrast agent, the deposition of a thin uniform film of a low-density material such as C after each corrective layer would be an alternative approach that can be applied on any given material.

##### 4.2. Film stress

As indicated in Section 3.3, the substrate-curvature change after corrective Cr coatings is a serious obstacle to fully exploit the potential of DD and to improve the surface figure down to the nanometre scale. Assuming that the observed curvature change after the first iteration shown in Fig. 6 is entirely caused by film stress, using the Young's modulus of the Pyrex substrate of 63 GPa (Matweb, 2019) and applying the Stoney equation (Stoney, 1909) one obtains an equivalent tensile stress of about 2.5 GPa. To investigate the contribution of stress in the growing Cr film, the substrate curvature of thin Si and glass sheets was measured *in situ* with the Cr thickness increasing up to 300 nm. It was found that Cr develops a tensile stress of 0.3–0.6 GPa in the relevant thickness range of 50–150 nm, in good agreement with the literature data (Misra & Nastasi, 1999), but five times lower than what would be needed to explain the observed mirror-curvature change. The sample curvature evolution was monitored as a function of time in a vacuum and after exposure to air in order to evaluate potential relaxation and oxidation effects. An additional curvature modification of about 50% on top of the growth-related effects was observed, still leaving a factor of 3 compared with the observations in Section 3.3. The curvature evaluation of nearly flat mirrors from LTP data is highly sensitive to the choice of the analysis length and to the involved data treatment. The resulting limited accuracy may explain the observed contradiction. Nevertheless, film stress during DD remains an issue and needs to be taken into account. Possible mitigation approaches might be to apply an equivalent coating on the rear face of the mirror.

##### 4.3. Surface roughness

An important aspect in DD is the question of to what extent the method can maintain the initial surface roughness of the substrate. Rough surfaces cause diffuse scattering and penalize the growth of low *d*-spacing MLs. A series of Cr films with thicknesses from 5 to 200 nm were deposited on Si wafers and studied with micro-interferometry (50× objective), XRR and SEM imaging. Fig. 8 shows the Cr surface roughness versus thickness measured with interferometry (blue dots) and XRR (red dots). While the interferometer data show no significant roughness evolution, the XRR spectra suggest a linear increase of the surface roughness with growing Cr thickness. These findings are confirmed by a series of high-resolution SEM images shown in Fig. 9. The surface of the 10 nm-thick Cr film [image (a)] appears smooth and uniform. At  $t(\text{Cr}) = 30$  nm [image (b)] a weak texture is visible that evolves and amplifies when the Cr thickness increases to 100 nm [image (c)] and 200 nm [image (d)]. The characteristic surface structure is probably linked to crystallization phenomena and columnar growth in thick Cr films that generate grain sizes of

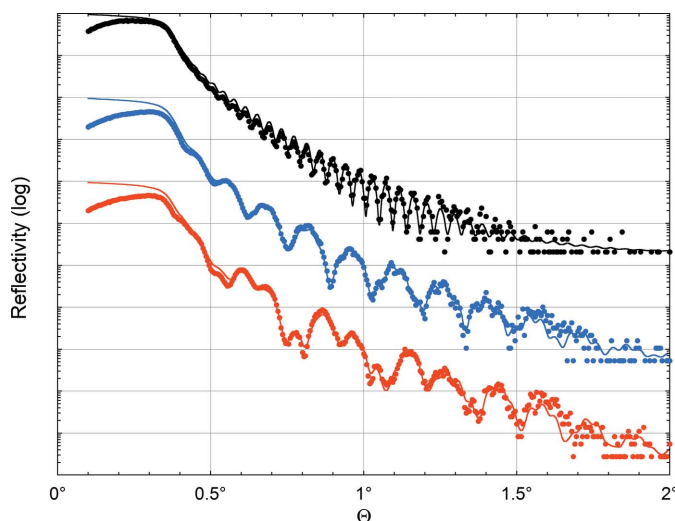


**Figure 7** XRR spectra versus angle  $\Theta$  of three successive Cr coatings of variable thickness, starting with the top (black), followed by the centre (blue) and finished by the bottom curve (red). Dots indicate experimental data, solid lines show simulations. The datasets are vertically shifted for better visibility.

the order of 20 nm (Misra & Nastasi, 1999). Their size is below the lateral resolution of the micro-interferometer and explains why they remain undetected in this instrument. The detrimental impact of the increasing roughness was confirmed by

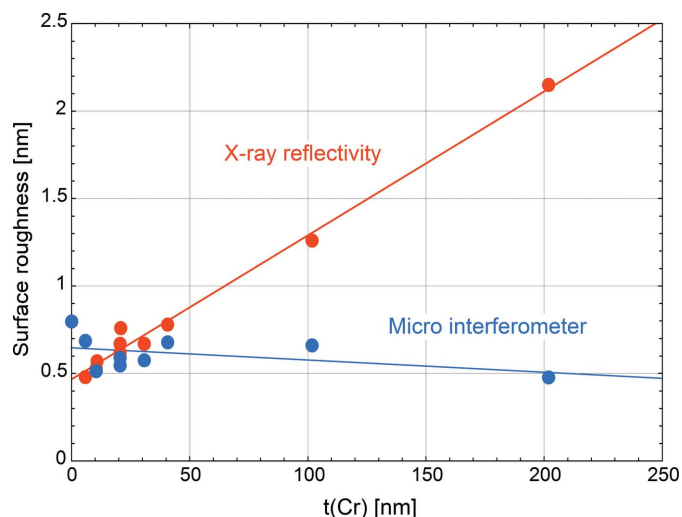


**Figure 8**  
Cr surface roughness versus thickness measured with a micro-interferometer (blue dots) and deduced from XRR (red dots). Solid lines are linear fits to the data.

the deposition of short-period W/B<sub>4</sub>C MLs on the samples whose performance dropped for  $t(\text{Cr}) > 20$  nm. All roughness data shown here were obtained from Cr coatings on Si wafers with an original surface roughness of about 0.5 nm (RMS). Although the roughness of the corrected mirror substrate was lower [0.3 nm (RMS)], the observed evolution with Cr thickness was similar.

### 5. Summary

A DD technique based on DC magnetron sputtered Cr layers and off-line XRR metrology was developed to improve the figure of reflective X-ray optics on length scales of 30 mm and above. The method achieves a convergence rate of >95% per iteration using up to 100 nm-thick coatings. However, in the given case, considerable mirror-curvature changes limited the improvement to a factor of 7 after two iterations. Part of this phenomenon can be explained by stress in the Cr films, as well as by tolerances of the available surface metrology, but further investigations will be necessary to fully understand these findings. At present, the observed roughness evolution restricts the application of the DD process to Cr thicknesses up to 20 nm, in particular in the context of short-period ML coatings. During future work, thicker and stiffer Si substrates

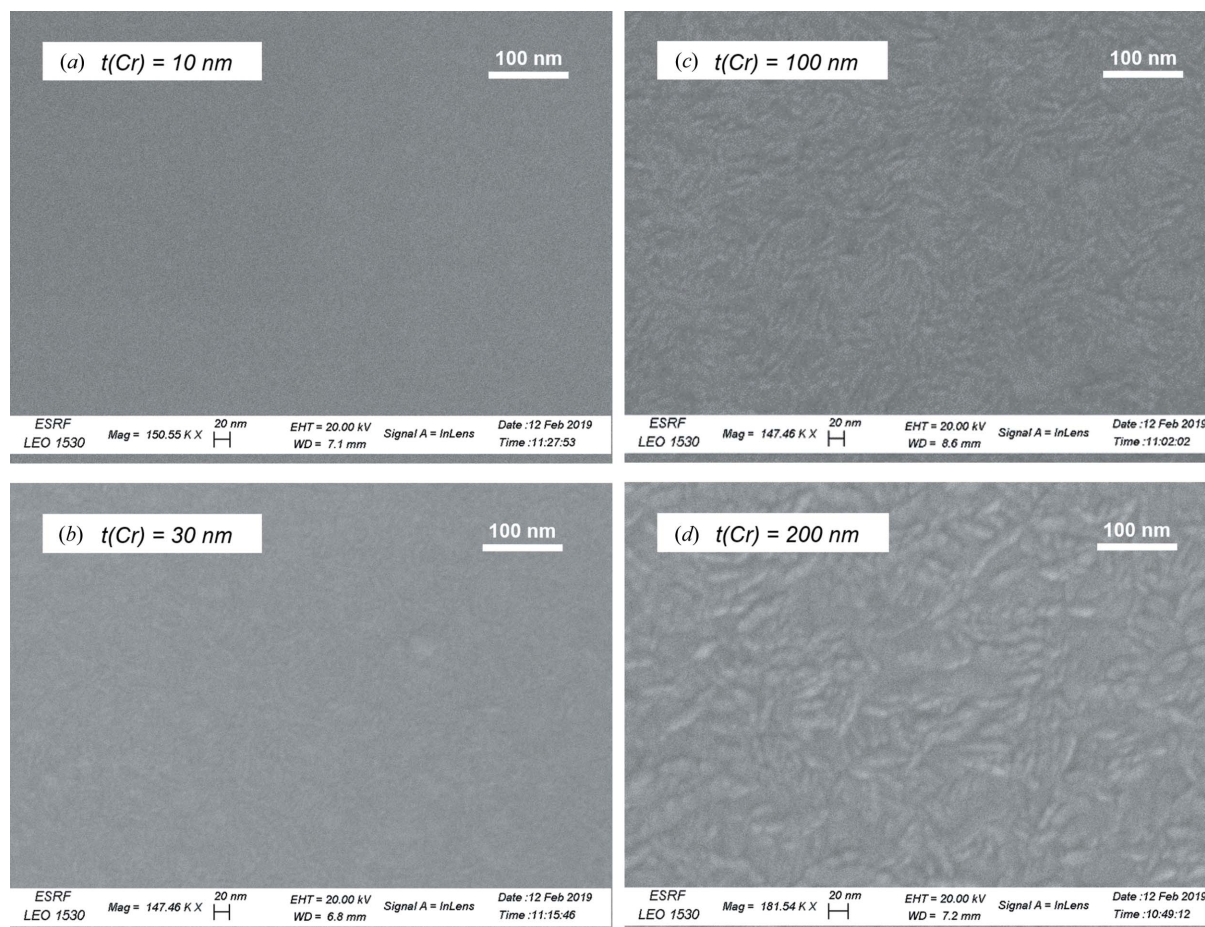


**Figure 9**  
High-resolution SEM images of Cr films with thicknesses of 10 nm (a), 30 nm (b), 100 nm (c) and 200 nm (d).

with smaller initial figure errors will be used to reduce the potential impact of film stress. Optimized Cr deposition parameters, alternative materials or auxiliary layers may reduce both the growth stress and the surface roughness. The feasibility to correct height errors on length scales of a few millimetres will be studied using narrower beam apertures.

### Acknowledgements

The authors would like to acknowledge I. Snigireva for SEM imaging.

### References

- Alcock, S. G. & Cockerton, S. (2010). *Nucl. Instrum. Methods Phys. Res. A*, **616**, 110–114.
- Arnold, T., Böhm, G., Fechner, R., Meister, J., Nickel, A., Frost, F., Hänsel, T. & Schindler, A. (2010). *Nucl. Instrum. Methods Phys. Res. A*, **616**, 147–156.
- Atkins, C., Kilaru, K., Ramsey, B. D., Broadway, D. M., Gubarev, M. V., O'Dell, S. L. & Zhang, W. W. (2015). *Proc. SPIE*, **9603**, 96031G.
- Handa, S., Mimura, H., Yumoto, H., Kimura, T., Matsuyama, S., Sano, Y. & Yamauchi, K. (2008). *Surf. Interface Anal.* **40**, 1019–1022.
- Kilaru, K., Gregory, D. A., Ramsey, B. D. & Gubarev, M. V. (2011). *Opt. Eng.* **50**, 106501.
- Matsuyama, S., Inoue, T., Yamada, J., Kim, J., Yumoto, H., Inubushi, Y., Osaka, T., Inoue, I., Koyama, T., Tono, K., Ohashi, H., Yabashi, M., Ishikawa, T. & Yamauchi, K. (2018). *Sci. Rep.* **8**, 17440.
- Matweb (2019). *Corning Pyrex 7740 Borosilicate Glass Sheet*, <http://matweb.com/search/datasheet.aspx?MatGUID=5bb651ca58524e79a503011b2cd8083d&ckck=1>.
- Misra, A. & Nastasi, M. (1999). *J. Mater. Res.* **14**, 4466–4469.
- Morawe, Ch., Barrett, R., Friedrich, K., Klünder, R. & Vivo, A. (2011). *Proc. SPIE*, **8139**, 813909.
- Morawe, Ch., Borel, Ch. & Peffen, J. Ch. (2007). *Proc. SPIE*, **6705**, 670504.
- Morawe, Ch. & Peffen, J. Ch. (2009). *Proc. SPIE*, **7448**, 74480H.
- Morawe, Ch., Peffen, J. Ch. & Friedrich, K. (2010). *Proc. SPIE*, **7802**, 78020B.
- Morawe, Ch., Peffen, J. Ch. & Pakawanit, P. (2018). *Proc. SPIE*, **10760**, 1076005.
- Parratt, L. G. (1954). *Phys. Rev.* **95**, 359–369.
- Rommeveaux, A., Thomasset, M. & Cocco, D. (2008). *Modern Developments in X-ray and Neutron Optics*, edited by Alexei Erko, Moudrad Idir, Thomas Krist and Alan G. Michette, Vol. 137, *Springer Series in Optical Sciences*, pp. 181–191. Berlin, Heidelberg: Springer-Verlag.
- Stoney, G. G. (1909). *Proc. R. Soc. London Ser. A*, **82**, 172–175.
- Varosi, F. (1992). *NASA/GSFC, The IDL Astronomy User's Library*, <https://idlastro.gsfc.nasa.gov>.
- Wang, T., Huang, L., Vescovi, M., Kuhne, D., Tayabaly, K., Bouet, N. & Idir, M. (2019). *Opt. Express*, **27**, 15368–15381.
- Yamauchi, K., Mimura, H., Inagaki, K. & Mori, Y. (2002). *Rev. Sci. Instrum.* **73**, 4028–4033.
- Yamauchi, K., Mimura, H., Kimura, T., Yumoto, H., Handa, S., Matsuyama, S., Arima, K., Sano, Y., Yamamura, K., Inagaki, K., Nakamori, H., Kim, J., Tamasaku, K., Nishino, Y., Yabashi, M. & Ishikawa, T. (2011). *J. Phys. Condens. Matter*, **23**, 394206.